Mechanism of formation of an inverse energy flow in a sharp focus

V. V. Kotlyar, S. S. Stafeev, A. G. Nalimov, A. A. Kovalev, and A. P. Porfirev

Image Processing Systems Institute of RAS—Branch of the FSRC "Crystallography and Photonics" RAS, Samara, 443001, Russia
and Samara National Research University, Samara, 443086, Russia

A reverse energy flow is theoretically demonstrated to occur in the interference pattern generated by four plane waves with linear polarization. In some regions of the interference pattern, the right-handed triplets of plane-wave vectors **k** ($k_z > 0$), **E**, and **H** (comprising a wave vector and **E**- and **H**-field vectors) sum up to form an electromagnetic field described by a right-handed triplet of vectors **k** ($k_z < 0$), **E**, and **H**. It is in these regions that the negative propagation of light occurs. On the optical axis the orbital energy flow, proportional to the light intensity, is shown to be positive, while the spin flow is negative and exceeds the orbital flow in magnitude. That is why the on-axis summary energy flow is negative. The magnitude of the reverse flow on the optical axis is two times lower than that of the intensity. A similar mechanism may apply to the case of sharply focusing a laser beam with second-order polarization or phase singularity. Using two identical micro-objectives with a numerical aperture of 0.95, it has been demonstrated experimentally that the intensity on the optical axis near the focus of an optical vortex with a topological charge of 2 is zero for right circular polarization and nonzero for left circular polarization. This confirms that in the latter case there is the reverse flow of light energy on the optical axis, since in the center of the measured energy flow distribution there is a very weak local maximum (the Arago spot) aroused due to diffraction of the forward flow by a circle with a diameter of 300 nm (the diameter of the tube with the reverse flow). Comparing the numerical and experimental intensity distributions, it is possible to determine the diameter of a "tube" with the reverse flow. For a numerical aperture of 0.95 and a wavelength of 532 nm, the diameter of the tube of the reverse flow along the optical axis is 300 nm. It is also shown experimentally that when an optical beam with second-order cylindrical polarization is focused with a numerical aperture of 0.95, there is a circularly symmetric energy flow in the focus with a very weak flow in the center (the Arago spot), whose distribution is determined by diffraction of the forward flux by an ∼300-nm-diameter circular area, where the energy flow is reverse. This also confirms that in the latter case, there is a reverse energy flow on the optical axis.

I. INTRODUCTION

Optical vortex beams, which have been around for quite a long time [1], have a spiral phase that affects their propagation properties [2]. Optical vortices have attracted the steady interest of researchers due to their extremely wide applications potential. By way of illustration, laser vortex beams have been utilized in an optical vortex coronagraph when searching for exoplanets [3], as optical tweezers for trapping and manipulating microparticles [4,5], and as an optical spanner for rotating and transferring orbital angular momentum to particles [6,7]. They show promise for optical communications for improving data carrying capacity [8], quantum computing [9,10], and high-resolution electron microscopy [11]. One more potential application for the optical vortices is associated with the existence of regions with negative propagation of light [12–14]. We have recently shown [12] that a reverse energy flow occurs in the sharp focus of an optical vortex whose integer topological charge is larger than unity. We have also demonstrated theoretically and numerically [13] that in the sharp focus of a circularly polarized optical vortex with topological charge $m = 2$, there exists a near-axis reverse energy flow, which is comparable in magnitude with the incident energy. The presence of an on-axis reverse energy

flow in the focus of a second-order polarization vortex has also been demonstrated numerically [14]. It has been shown that the negative propagation of light can be achieved using a metalens [15].

Earlier, the effect of the negative propagation of light was studied by a number of researchers. In particular, according to a simple expression derived in Ref. [16] to describe the on-axis component of the Poynting vector in an aplanatic system when focusing a plane linearly polarized wave, a reverse energy flow occurs on some circumferences around dark rings (intensity minima). Although the energy backflow was also discovered in superposition of four plane waves [17], the author discarded the result as being physically meaningless. Focusing a paraxial Gaussian beam with a limited-aperture spherical lens has been numerically shown to produce, in and near the focal plane, dark Airy rings featuring phase singularity [18]. Later on, Berry utilized asymptotics techniques to show that such singularities also occurred in the focus of a nonparaxial Gaussian beam focused by an open-aperture lens [19]. A circulating energy flow was shown to occur around phase singularity, which contained a reverse flow [19]. Volyar has numerically shown [20] that linearly polarized nonparaxial vector Gaussian beams (or lower-order spherical modes) form an elliptic focal spot surrounded by

"singularity isles" (instead of Airy rings), near which a reverse energy flow was observed. Analogous singularity isles and reverse energy flows were discovered [21] in the focal plane of circularly polarized nonparaxial vector Gaussian beams. Considering a simple example of the interference of two coaxial Gaussian beams, a toroidal energy flow, including the reverse one, has been shown [22] to occur around a ring-shaped intensity null. Note that the reverse flows reported in Refs. [16–22] were low in magnitude and observed in small peripheral off-axis regions. Meanwhile, in Ref. [23] it was demonstrated that superposition of two coaxial vector Bessel TE and TM waves could produce an on-axis reverse flow of energy. An optical tractor concept, when the force exerted upon a particle is opposite to the incident beam, has also been proposed [24,25]. The presence of the reverse energy flow has been shown to not always result in a negative force, and vice versa, the force pushing a particle backward may appear in the absence of a reverse flow. The negative propagation of energy in a vector fractional-order Bessel beam has been numerically demonstrated [26]. Such an optical beam is actually a linear combination of a countable number of conventional Bessel modes. Energy flow characteristics for vector X waves and necessary conditions for the negative propagation of light have been theoretically deduced [27]. The presence of the reverse flow of energy has been numerically shown to occur for nonparaxial two-dimensional (2D) Airy beams and nonparaxial parabolic vector Weber beams [28,29]. Theoretical conditions to be imposed on a light field, making it possible to create local regions of "optical retropropagation" (i.e., the reverse energy flow), have also been derived [30]. From the review above, vortex laser beams are seen to be most popular for obtaining the negative propagation of light energy, with circular polarization of light being the necessary condition.

Our conjecture is that the negative propagation of light (or reverse energy flow) can also take place in light fields with phase and polarization singularities, which produce vortex knots in space [31–33].

This work is an attempt to offer a mechanism behind the generation of regions of the negative propagation of light predicted in Refs. [12–15]. Using a simple example of the interference of four plane waves [17] with specially tailored linear polarization states, we show in detail in which way the reverse energy flow is generated. Formulas to define the magnitude of the reverse flow versus the angle between the interfering plane waves are derived. Coordinates and areas are derived of all regions in which the negative propagation of light is observed. We also show the four-plane-wave model proposed here to account well for the on-axis reverse energy flow in the sharp focus of the optical vortex with second-order polarization reported in Ref. [14].

Using two identical micro-objectives with a numerical aperture of 0.95, we measure the energy flow distribution in the sharp focus of a circularly polarized optical vortex with a topological charge of 2 as well as in the focus of a Gaussian beam with second-order cylindrical polarization. In both cases, a similar distribution of the energy flow is obtained, with a weak local maximum (a saddle point, to be exact) formed in the center due to diffraction of the direct flow by a circle (about 300 nm in diameter), which bounds a tube
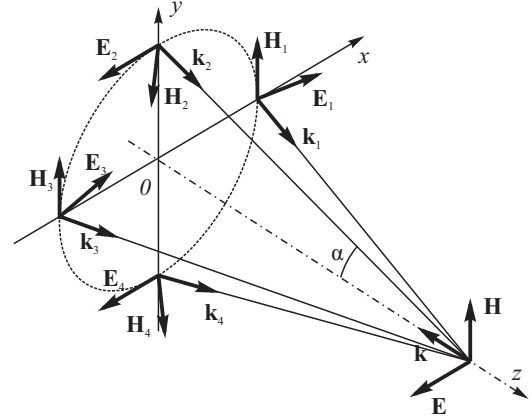

FIG. 1. Schematic of superposition of four linearly polarized plane waves.

of the reverse flow along the optical axis. This is proof of the existence and reality of the reverse energy flow.

In conclusion, we show that a spherical conductive nanoparticle placed on the optical axis in the reverse flow region moves oppositely to the incident beam. Thus, the reverse energy flow in the sharp focus of an optical vortex in Ref. [14] is shown to be high enough to produce a dissipative force pushing the microparticle backward.

II. INTERFERENCE OF FOUR LINEARLY POLARIZED PLANE WAVES

Let us analyze an interference pattern of four coherent monochromatic plane waves with specially tailored linear polarization states in Fig. 1. The E-vectors of the four plane waves are given by

$$
\begin{aligned}
\mathbf{E}_1 &= (\mathbf{e}_x \cos\alpha + \mathbf{e}_z \sin\alpha)\exp(-ikx\sin\alpha + ikz\cos\alpha), \\
\mathbf{E}_2 &= -\mathbf{e}_x \exp(-iky\sin\alpha + ikz\cos\alpha), \\
\mathbf{E}_3 &= (\mathbf{e}_x \cos\alpha - \mathbf{e}_z \sin\alpha)\exp(ikx\sin\alpha + ikz\cos\alpha), \\
\mathbf{E}_4 &= -\mathbf{e}_x \exp(iky\sin\alpha + ikz\cos\alpha),
\end{aligned}
\tag{1}
$$

where (x, y, z) are the Cartesian coordinates, $(\mathbf{e}_x, \mathbf{e}_y, \mathbf{e}_z)$ is the right-handed triplet of unit coordinate vectors, k is the wave number of light, and α is the angle of the incident waves with the optical axis z. From Maxwell's equation for a monochromatic field,

$$
\mathrm{rot}\mathbf{E} = ik\mathbf{H},
\tag{2}
$$

the magnetic field vectors $\mathbf{H}_n$, $n = 1, 2, 3, 4$ for the four waves can be written as

$$
\begin{aligned}
\mathbf{H}_1 &= \mathbf{e}_y \exp(-ikx\sin\alpha + ikz\cos\alpha), \\
\mathbf{H}_2 &= -(\mathbf{e}_y \cos\alpha + \mathbf{e}_z \sin\alpha) \\
&\quad \times \exp(-iky\sin\alpha + ikz\cos\alpha), \\
\mathbf{H}_3 &= \mathbf{e}_y \exp(ikx\sin\alpha + ikz\cos\alpha), \\
\mathbf{H}_4 &= -(\mathbf{e}_y \cos\alpha - \mathbf{e}_z \sin\alpha) \\
&\quad \times \exp(iky\sin\alpha + ikz\cos\alpha).
\end{aligned}
\tag{3}
$$

From (1) and (3), the intensity distribution of the E field is given by

$$
\begin{aligned}
I_\alpha = |E_x|^2 + |E_z|^2 = 4\{&[\cos\alpha\cos(kx\sin\alpha) - \cos(ky\sin\alpha)]^2 \\
&+ \sin^2\alpha\sin^2(kx\sin\alpha)\}.
\end{aligned}
\tag{4}
$$

When the four plane waves of interest are superimposed at a large angle ($\alpha \to \pi/2$), Eq. (4) can be approximately replaced by

$$I_{\pi/2} \approx 4(\cos^2 ky + \sin^2 kx). \tag{5}$$

From (5), the intensity maxima of the interference pattern of the four plane waves are seen to be staggered and located near points with the coordinates

$$\begin{aligned} (x_p, y_q) &= [\lambda(2p+1)/4, \ \lambda q/2], \\ p, q &= 0, \ \pm 1, \ \pm 2 \cdots . \end{aligned} \tag{6}$$

From (1) and (3), we can also derive components of the Poynting vector (energy flow vector) defined as

$$\mathbf{S} = \tfrac{1}{2}\mathrm{Re}[\mathbf{E} \times \mathbf{H}^*], \tag{7}$$

where Re is the real part of the number and * denotes the complex conjugation. Substituting Eqs. (1) and (3) into Eq. (7), we derive the longitudinal component of the Poynting vector S_z in the following form:

$$\begin{aligned} S_{z,\alpha} = {}& 2\cos\alpha[\cos^2(kx\sin\alpha) + \cos^2(ky\sin\alpha)] \\ & - 2(1 + \cos^2\alpha)\cos(kx\sin\alpha)\cos(ky\sin\alpha). \end{aligned} \tag{8}$$

From Eq. (8), the reverse energy flow is seen to be absent when the plane waves are converging at a small angle ($\alpha \to 0$), because

$$S_{z,\alpha \to 0} \approx 2[\cos(kx\alpha) - \cos(ky\alpha)]^2 \geqslant 0. \tag{9}$$

Meanwhile, Eq. (8) suggests that when waves converge at large angles ($\alpha \to \pi/2$), regions of the reverse energy flow will be found in the interference pattern, and they are staggered:

$$S_{z,\alpha \to \pi/2} = -2\cos(kx)\cos(ky). \tag{10}$$

From Eq. (10), the energy backflow in the cross section of the interference pattern is seen to have its maxima near points given by

$$\begin{aligned} (x_p, y_q) &= (\lambda p, \ \lambda q), \quad p, q = 0, \pm 1, \pm 2 \cdots , \\ (x_p, y_q) &= [\lambda(p+1/2), \ \lambda(q+1/2)]. \end{aligned} \tag{11}$$

It is worth noting that whatever the convergence angle α, a nonzero intensity and reverse energy flow will be found on the optical axis at the center of the interference pattern:

$$\begin{aligned} I_\alpha(x = y = 0) &= 4(1 - \cos\alpha)^2, \\ S_{z,\alpha}(x = y = 0) &= -2(1 - \cos\alpha)^2. \end{aligned} \tag{12}$$

The maximal energy flow in the interference pattern is

$$S_{z,\alpha}\left[x = \frac{\lambda(2p+1)}{2\sin\alpha}, \ x = \frac{\lambda(2q)}{2\sin\alpha}\right] = 2(1 + \cos\alpha)^2. \tag{13}$$

Note that Eq. (13) also holds for points with the coordinates:

$$x = \frac{\lambda p}{\sin\alpha}, \quad y = \frac{\lambda(q+1/2)}{\sin\alpha}.$$

As α tends to $\pi/2$, the maximum value of the incident energy flow becomes equal to that of the reverse flow, approaching 2 (from above and below).

Figure 2 depicts patterns of (a) the energy density and (b) the Poynting vector magnitude across the interference pattern
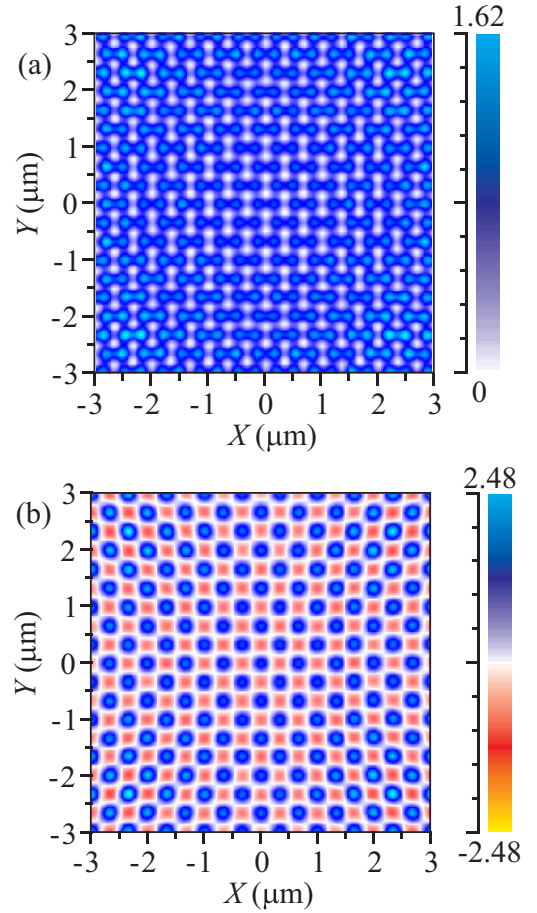

FIG. 2. Patterns of (a) the energy density and (b) the axial projection of the Poynting vector S_z for the four 633-nm plane waves of Eqs. (1) and (3) with the convergence angle $\alpha = 80°$. The regions of the reverse energy flow are shown in red (b).

of the four plane waves given by Eqs. (1) and (3) at distance $z = 0$ and at $\alpha = 80°$. The patterns in Fig. 2 were obtained via the Finite-Difference Time Domain method (FDTD)-aided rigorous solution of Maxwell's equations.

From Eq. (7), the transverse components of the Poynting vector are seen to equal zero, meaning that the intensity pattern and energy flow distribution in Fig. 2 are the same at any z.

From Eqs. (1), (3), and (7), the vectors $\mathbf{S}$, $\mathbf{E}$, and $\mathbf{H}$ are seen to form a left-handed (rather than right-handed) triplet on the optical axis ($x = y = 0$), meaning that the energy flow and the wave vector $\mathbf{k}$ are directed oppositely to the z axis. Actually, on the optical axis in Fig. 1 we have

$$\begin{aligned} \mathbf{E}(x = y = 0) &= \mathbf{E}_1 + \mathbf{E}_2 + \mathbf{E}_3 + \mathbf{E}_4 \\ &= -2\mathbf{e}_x(1 - \cos\alpha)\exp(ikz\cos\alpha), \\ \mathbf{H}(x = y = 0) &= \mathbf{H}_1 + \mathbf{H}_2 + \mathbf{H}_3 + \mathbf{H}_4 \\ &= 2\mathbf{e}_y(1 - \cos\alpha)\exp(ikz\cos\alpha), \\ \mathbf{S}(x = y = 0) &= -2\mathbf{e}_z(1 - \cos\alpha)^2. \end{aligned} \tag{14}$$

Shown in Fig. 3 for visual purposes are the right-handed triplet of the Cartesian unit vectors ($\mathbf{e}_x$, $\mathbf{e}_y$, $\mathbf{e}_z$) and the right-handed triplet of the on-axis vectors $\mathbf{S}$ ($S_z < 0$), $\mathbf{E}$, and $\mathbf{H}$.
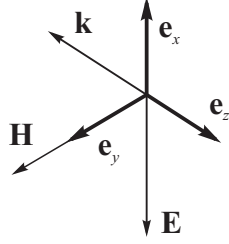
FIG. 3. Right-handed triplet of Cartesian unit vectors and the right-handed triplet of the on-axis vectors **k**, **E**, and **H** of a light field.

It is known [34] that the energy flow **S** consists of the orbital energy flow $\mathbf{S}_{or}$ and spin flow $\mathbf{S}_{sp}$:

$$\mathbf{S} = \frac{1}{2}\mathrm{Re}[\mathbf{E} \times \mathbf{H}^*] = \frac{1}{2k}\mathrm{Im}[\mathbf{E}^*(\nabla)\mathbf{E}]$$
$$+ \frac{1}{4k}\{\nabla \times \mathrm{Im}[\mathbf{E}^* \times \mathbf{E}]\} = \mathbf{S}_{or} + \mathbf{S}_{sp}. \tag{15}$$

For four plane waves from Eq. (1), axial components of the orbital energy flow and of the spin flow are given by

$$\begin{aligned} S_{sp,z} &= 2\sin^2\alpha[-\cos(kx\sin\alpha)\cos(ky\sin\alpha) \\ &\quad + 2\cos\alpha\cos(2kx\sin\alpha)], \\ S_{or,z} &= 2\cos\alpha[(\cos\alpha\cos(kx\sin\alpha) - \cos(ky\sin\alpha))^2 \\ &\quad + 2\sin^2\alpha\sin^2(kx\sin\alpha)] = \frac{\cos\alpha}{2}I_\alpha \geqslant 0. \end{aligned} \tag{16}$$

It can be shown that the sum $S_{sp,z} + S_{or,z}$ from Eq. (16) equals the energy flow from Eq. (8). According to Eq. (16), the orbital energy flow is proportional to the intensity (4) and can be only positive. On the optical axis, the orbital energy flow is positive, while the spin flow is negative and exceeds the orbital flow by magnitude:

$$\begin{aligned} S_{sp,z}(x=y=0) &= -2\sin^2\alpha(1-\cos\alpha) < 0, \\ S_{or,z}(x=y=0) &= 2\cos\alpha(1-\cos\alpha)^2 \geqslant 0. \end{aligned} \tag{17}$$

Therefore, the total energy flow (12) on the optical axis is negative. With increasing angle α from Eq. (17), the orbital flow decreases to zero, while the spin flow reaches its maximal value.

The axial spin flow $\mathbf{S}_{sp}$ for four linearly polarized plane waves occurs due to a $\pi/2$ phase shift between the X and Z components of the electric field (1) (in the XZ plane, polarization is elliptic, "photonic wheels"). Therefore, the spin density vector [34]

$$\mathbf{s}_E = \frac{1}{4}\mathrm{Im}[\mathbf{E}^* \times \mathbf{E}] \tag{18}$$

has only the Y component:

$$\begin{aligned} s_{E,y} &= 2\sin\alpha\sin(kx\sin\alpha) \\ &\quad \times[\cos\alpha\cos(kx\sin\alpha) - \cos(ky\sin\alpha)]. \end{aligned} \tag{19}$$

III. GENERATION OF A REVERSE ON-AXIS ENERGY FLOW IN THE FOCUS OF A LIGHT BEAM WITH POLARIZATION SINGULARITY

Hereafter, the light field with arbitrary-order polarization singularity is referred to as a polarization vortex. In this section, we show that similar to explaining the existence of the reverse flow by interference of four plane waves, the

same mechanism applies to the generation of a reverse energy flow in the focus of a polarization vortex. Sharply focusing a polarization vortex has been reported earlier [35]. In such a polarization vortex, the initial Jones vector (Fig. 4) is given by

$$\mathbf{E} = \begin{pmatrix} -\sin 2\varphi \\ \cos 2\varphi \end{pmatrix}, \quad \mathbf{H} = \begin{pmatrix} -\cos 2\varphi \\ -\sin 2\varphi \end{pmatrix}, \tag{20}$$

where φ is the azimuthal angle of a cylindrical coordinate system (r, φ, z).

Shown in Fig. 4(a) is a pattern of polarization vectors across the original second-order polarization vortex $\lambda = 532$ nm, which was focused with an aplanatic system with numerical aperture NA = 0.95. Shown in Fig. 4(b) is a near-focus intensity pattern in the plane (y, z), with arrows denoting the direction of the energy flow **S**. According to Fig. 4(e), two intensity nulls coincide with the points of zero reverse flow. Therefore, a tube of the reverse flow along the optical axis has a diameter of about 300 nm [Fig. 4(e)].

Using Richards-Wolf formulas it has been shown [35] that in the focal plane of the field (20) generated by an aplanatic optical system (in the form of an ideal spherical lens), components of the electric and magnetic field vectors are given by

$$\begin{aligned} E_x &= -i\sin 2\varphi I_{0,2}, \\ E_y &= -i(-\cos 2\varphi I_{0,2} + I_{2,0}), \\ E_z &= 2\sin\varphi I_{1,1}, \\ H_x &= -i(\cos 2\varphi I_{0,2} + I_{2,0}), \\ H_y &= -i\sin 2\varphi I_{0,2}, \\ H_z &= 2\cos\varphi I_{1,1}. \end{aligned} \tag{21}$$

Designations in (21) stand for

$$I_{0,2} = \frac{\pi f}{\lambda}\int_0^\alpha \sin\theta\cos^{1/2}\theta(1+\cos\theta)A(\theta)e^{ikz\cos\theta}J_2(x)d\theta,$$

$$I_{2,0} = \frac{\pi f}{\lambda}\int_0^\alpha \sin\theta\cos^{1/2}\theta(1-\cos\theta)A(\theta)e^{ikz\cos\theta}J_0(x)d\theta,$$

$$I_{1,1} = \frac{\pi f}{\lambda}\int_0^\alpha \sin^2\theta\cos^{1/2}\theta A(\theta)e^{ikz\cos\theta}J_1(x)d\theta. \tag{22}$$

In (22), $x = kr\sin\theta$, $J_m(x)$ is an mth order Bessel function, $A_m(\theta)$ is a real function of the amplitude distribution in the input pupil of the aplanatic system, and NA = $\sin\alpha$ and f are the numerical aperture and the focal length of the aplanatic system.

From Eq. (21), the transverse intensity distribution and the longitudinal component of the Poynting vector read as

$$I_\perp = I_{0,2}^2 + I_{2,0}^2 - 2\cos 2\varphi(I_{0,2}I_{2,0}), \quad S_z = \frac{1}{2}(I_{0,2}^2 - I_{2,0}^2). \tag{23}$$

According to Eq. (23), the backflow of energy on the optical axis $(r = 0)$ is two times lower than the intensity [similar to Eq. (12)]: $S_z(r=0) = -I_\perp(r=0)/2 = -I_{2,0}^2/2$.

From (21), we infer that in the focal plane $(z = 0)$ the on-axis $(r = 0)$ electromagnetic field is described by a left-handed triplet of vectors:

$$\mathbf{E} = -i\mathbf{e}_y I_{2,0}, \quad \mathbf{H} = -i\mathbf{e}_x I_{2,0}, \quad \mathbf{S} = -\mathbf{e}_z I_{2,0}^2/2. \tag{24}$$
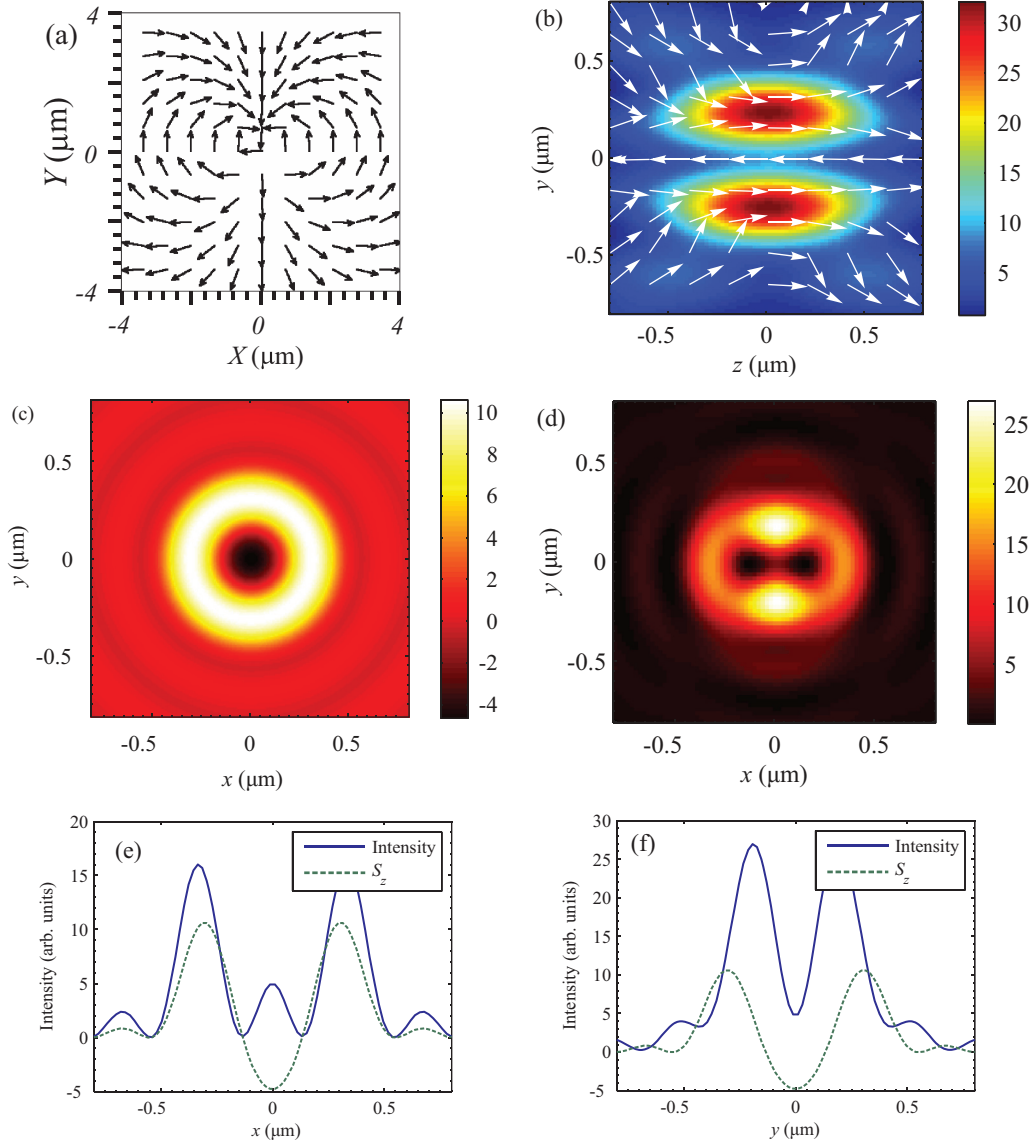
FIG. 4. (a) Pattern of polarization vectors in the original second-order polarization vortex, Eq. (20). (b) Near-focus intensity pattern in the plane (y, z). Arrows in (b) denote the energy flow direction **S**. (c) Distributions of the longitudinal component of the Poynting vector S_z. (d) Intensity in the focal plane and its cross sections along the axes x (e) and y (f). The intensity and the longitudinal component of the Poynting vector are plotted by the solid blue and dashed green curves, respectively.

Disregarding the imaginary unit, which defines the field phase jump by $\pi/2$ in the focus, the vector triplet in (24) is seen to be analogous to the vector triplet in (14), indicating that there is a reverse on-axis energy flow on the z axis [Fig. 4(b)].

Figure 5 depicts results of the FDTD-aided simulation for (a) the energy flux density, or the on-axis component S_z of the Poynting vector in the plane XZ, near the focus of second-order polarization vortex and (b) on-axis profiles of the electric and magnetic vectors. Analysis of Fig. 5(b) suggests that although the light field propagates in the positive direction of the z axis [from left to right in Fig. 5(b)], the vectors **E**, **H**, and **k** form a left-handed triplet of vectors near the optical axis, signifying the negative propagation of light in Fig. 5(b). By way of verifying that the reverse energy flow has a physical meaning, in the last section we calculate forces

exerted upon a conductive nanoparticle found on the optical axis near the focus [Figs. 4(b) and 5(a)].

IV. GENERATION OF A REVERSE ON-AXIS ENERGY FLOW IN THE FOCUS OF A LIGHT BEAM WITH PHASE SINGULARITY

A circularly polarized optical vortex with the topological charge $m = 2$ is given by [36]

$$\mathbf{E} = \frac{A(\theta)e^{i2\varphi}}{\sqrt{2}}\begin{pmatrix} 1 \\ i\sigma \end{pmatrix}, \quad \mathbf{H} = \frac{A(\theta)e^{i2\varphi}}{\sqrt{2}}\begin{pmatrix} -i\sigma \\ 1 \end{pmatrix}, \quad (25)$$

where $\sigma = 1$ for right-hand circular polarization and $\sigma = -1$ for left-hand circular polarization. When such a vortex is sharply focused, the electric and magnetic strength vectors
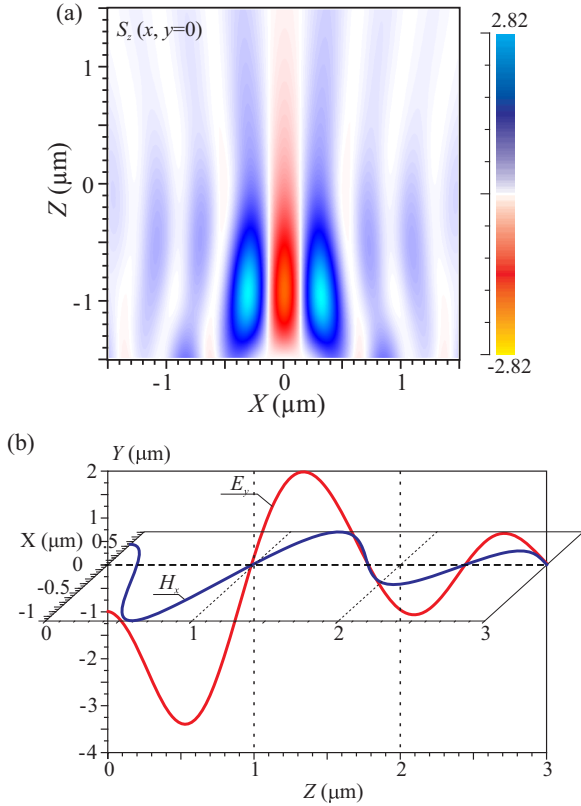
FIG. 5. (a) FDTD-aided pattern of the longitudinal component S_z for the Poynting vector in the plane ZX near the focus of a polarization vortex (Fig. 4) and (b) on-axis profiles of the E- and H-vectors, E_y, H_x.

have the following components near the focus [36]:

$$
\begin{aligned}
E_x &= i(e^{i2\varphi}I_{0,2} + \gamma_+ e^{i4\varphi}I_{2,4} + \gamma_- I_{2,0}), \\
E_y &= -1(\sigma e^{i2\varphi}I_{0,2} - \gamma_+ e^{i4\varphi}I_{2,4} + \gamma_- I_{2,0}), \\
E_z &= 2(\gamma_+ e^{i3\varphi}I_{1,3} - \gamma_- e^{i\varphi}I_{1,1}), \\
H_x &= \sigma e^{i2\varphi}I_{0,2} + \gamma_+ e^{i4\varphi}I_{2,4} - \gamma_- I_{2,0}, \\
H_y &= i(\sigma e^{i2\varphi}I_{0,2} - \gamma_+ e^{i4\varphi}I_{2,4} - \gamma_- I_{2,0}), \\
H_{1z} &= -2i(\gamma_+ e^{i3\varphi}I_{1,3} + \gamma_- e^{i\varphi}I_{1,1}),
\end{aligned}
\tag{26}
$$

where $\gamma_\pm = (1 \pm \sigma)/2$ $(\gamma_+ = \gamma_- = 1/\sqrt{2}$ at $\sigma = 0)$ and the following designations are introduced:

$$
I_{1,3} = \left(\frac{\pi f}{\lambda}\right) \int_0^\alpha \sin^2\theta \cos^{1/2}\theta A(\theta) e^{ikz\cos\theta} J_3(x) d\theta,
$$

$$
I_{2,4} = \left(\frac{\pi f}{\lambda}\right) \int_0^\alpha \sin\theta \cos^{1/2}\theta (1 - \cos\theta) A(\theta) e^{ikz\cos\theta} J_4(x) d\theta.
\tag{27}
$$

Based on Eq. (26), expressions can be derived for the intensity distribution of a right-hand $(\gamma_+ = 1,\ \gamma_- = 0)$ and left-hand $(\gamma_+ = 0,\ \gamma_- = 1)$ circularly polarized optical vortex in the focal plane:

$$
\begin{aligned}
I_{+2} &= I_{0,2}^2 + I_{2,4}^2 + 2I_{1,3}^2, \\
I_{-2} &= I_{0,2}^2 + I_{2,0}^2 + 2I_{1,1}^2.
\end{aligned}
\tag{28}
$$

Similarly, an expression can be obtained for the longitudinal component of the Poynting vector in the focal plane when focusing a right-hand or left-hand circularly polarized optical vortex with a topological charge $m = 2$:

$$
\begin{aligned}
S_{2z+} &= \tfrac{1}{2}\big(2I_{0,2}^2 - I_{2,4}^2\big), \\
S_{2z-} &= \tfrac{1}{2}\big(2I_{0,2}^2 - I_{2,0}^2\big).
\end{aligned}
\tag{29}
$$

The expression for S_{2z-} in Eq. (29) has a form similar to that of Eq. (23) for the flux in the focus of a light field with a second-order polarization singularity. A comparison of Eqs. (28) and (29) reveals that the intensity on the optical axis in the focus of a left-hand circularly polarized light is nonzero, whereas the longitudinal component of the energy flow is negative and two times lower than the intensity in magnitude:

$$
I_{-2}(r = 0) = I_{2,0}^2, \quad S_{-2z}(r = 0) = -\frac{I_{2,0}^2}{2}.
\tag{30}
$$

Equation (30) is quite identical to Eq. (12) for four plane waves.

According to Eq. (26), the right-handed triplet of electromagnetic-wave vectors on the optical axis is given by

$$
\mathbf{E} = iI_{2,0}\begin{pmatrix} 1 \\ i \end{pmatrix}, \quad \mathbf{H} = -I_{2,0}\begin{pmatrix} 1 \\ i \end{pmatrix}, \quad \mathbf{S} = -\mathbf{e}_z\frac{I_{2,0}^2}{2}.
\tag{31}
$$

Thus, it can be concluded that when focusing a left-hand circularly polarized optical vortex with the topological charge $m = 2$, the intensity on the optical axis near the focus is nonzero and the flow of light energy is negative. Similar to the interference of four plane waves (Fig. 1), an electromagnetic wave appears on the optical axis, whose electric and magnetic field strength vectors together with the Poynting vector $\mathbf{S}$ form a triplet of vectors (31), which describes a right-hand circularly polarized plane wave propagating along the axis z in the backward direction.

For a vortex field with left-hand circular polarization (26), the longitudinal component of the orbital energy flow (15) on the optical axis in the focal plane $(z = 0)$ reads as

$$
S_{or,z}(x = y = 0) = \tfrac{1}{2}I_{2,0}\tilde{I}_{2,0} > 0,
\tag{32}
$$

$$
\tilde{I}_{2,0} = \frac{\pi f}{\lambda} \int_0^\alpha \sin\theta \cos^{3/2}\theta (1 - \cos\theta) A(\theta) e^{ikz\cos\theta} J_0(x) d\theta,
\tag{33}
$$

while the longitudinal component of the spin flow vector on the optical axis is given by

$$
S_{sp,z}(x = y = 0) = -\tfrac{1}{2}I_{2,0}\tilde{I}_{1,0} < 0,
\tag{34}
$$

$$
\tilde{I}_{1,0} = \frac{\pi f}{\lambda} \int_0^\alpha \sin^3\theta \cos^{1/2}\theta A(\theta) e^{ikz\cos\theta} J_0(x) d\theta.
\tag{35}
$$

The total on-axis energy flow in the focus of a field (26) is equal to

$$
\begin{aligned}
S_z(x = y = 0) = S_{sp,z} + S_{or,z} &= -\tfrac{1}{2}I_{2,0}(\tilde{I}_{1,0} - \tilde{I}_{2,0}) \\
&= -\tfrac{1}{2}I_{2,0}^2 < 0,
\end{aligned}
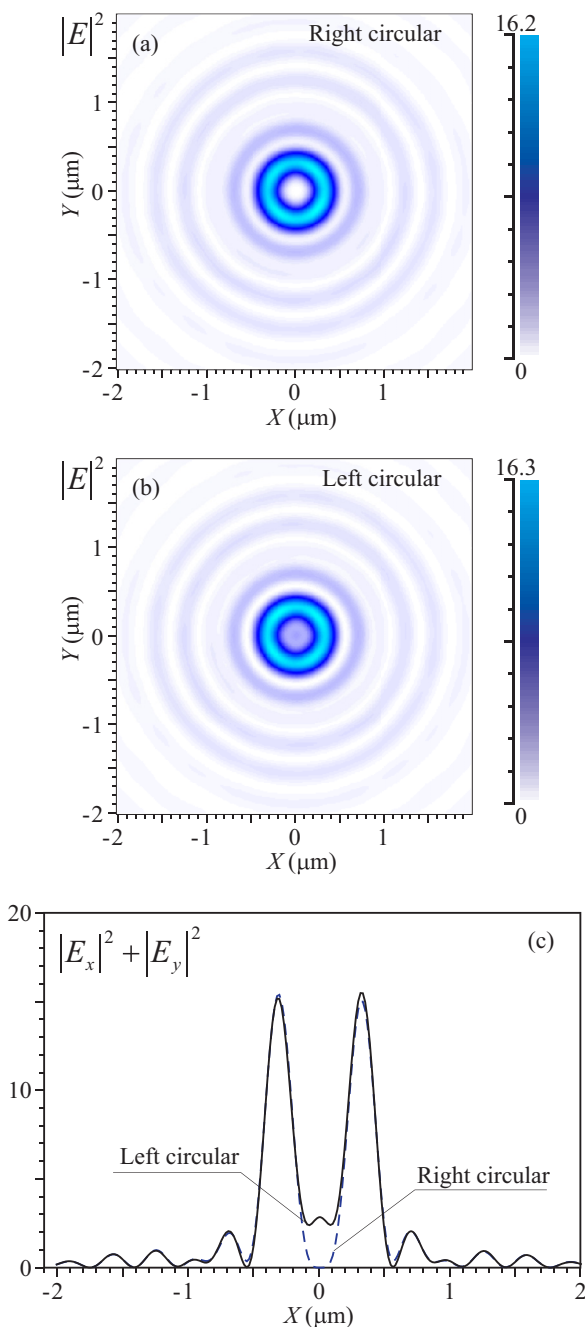\tag{36}
$$

and coincides with Eq. (30).

FIG. 6. Transverse intensity distributions calculated by the FDTD method in the focal plane of an optical vortex with a topological charge $m = 2$ with right (a) and left (b) circular polarization, as well as radial cross sections of intensity (c): right-hand polarization (dashed curve) and left-hand polarization (solid curve).
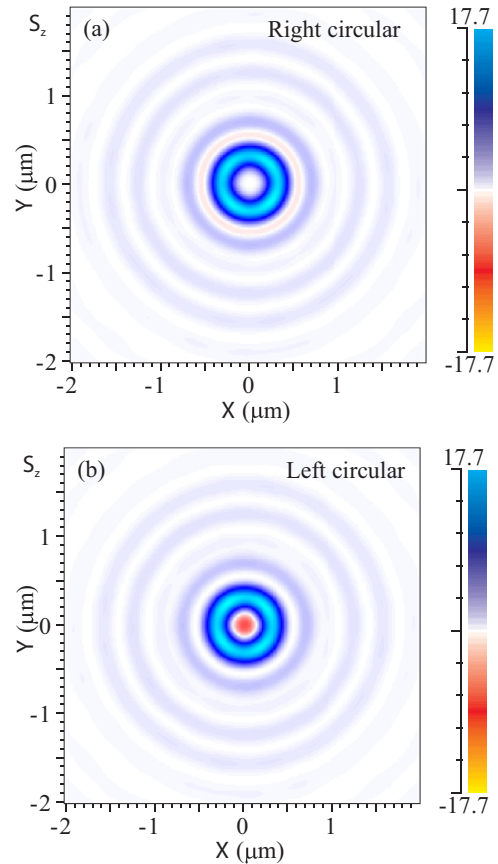

FIG. 7. Distributions of the longitudinal component of the Poynting vector calculated by the FDTD method in the focal plane of an optical vortex with the topological charge $m = 2$ with right (a) and left (b) circular polarization, as well as radial cross sections of the longitudinal component of the Poynting vector (c): right-hand polarization (solid curve) and left-hand polarization (dashed curve).

Figure 6 shows transverse intensity distributions $|E_x|^2 + |E_y|^2$ calculated by the FDTD method in the focal plane of an optical vortex (25) with right [Fig. 6(a)] and left [Fig. 6(b)] circular polarization. The focusing was done by a binary Fresnel zone plate with the numerical aperture NA = 0.95, radius $R = 4\,\mu$m, and focal length $f = 1.31\,\mu$m. The wavelength is $\lambda = 532$ nm and the distance between the grid points is $\lambda/30$.

According to Fig. 6(c), the intensity of the right-hand circularly polarized optical vortex on the optical axis ($x = 0$)

is zero near the focus, whereas the intensity of the left-hand circularly polarized optical vortex is nonzero.

Figure 7 shows distributions of the longitudinal component of the Poynting vector S_z obtained by the FDTD method in the focal plane of the optical vortex (26) with right-hand [Fig. 7(a)] and left-hand [Fig. 7(b)] circular polarization. Calculation parameters are the same as in Fig. 6.

As seen in Fig. 7(c), $S_z = 0$ on the optical axis ($x = 0$) in the focus of the right-hand circularly polarized optical vortex,
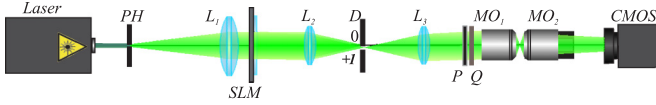
FIG. 8. Experimental setup. Laser: solid-state laser generating a linearly polarized Gaussian beam; PH: pinhole (with a 40-μm diameter); L$_1$, L$_2$, L$_3$: spherical lenses ($f_1 = 250$ mm, $f_2 = 150$ mm, $f_3 = 150$ mm); SLM: spatial light modulator (Holoeye LC 2012); D: diaphragm to block the zero diffraction order; P: polarizer; Q: quarter-wave plate; MO$_1$, MO$_2$: micro-objectives (Nikon 100 × /0.95 OFN25 WD0.3 CF Plan100×, NA = 0.95); CMOS: camera, ToupCam UCMOS08000KPB.

whereas for the left-hand circularly polarized optical vortex the flow is negative; $S_z < 0$. We note that the width of the light ring in focus in Figs. 6(c) and 7(c) is the same.

V. EXPERIMENTAL MEASUREMENT OF THE TRANSVERSE INTENSITY DISTRIBUTION IN THE SHARP FOCUS

Figure 8 shows a schematic of the experimental setup. A linearly polarized light from a solid-state laser ($\lambda = 532$ nm) is spatially filtered and collimated by a 40-μm-diameter pinhole PH and a spherical lens L$_1$ ($f_1 = 250$ mm). Then, the collimated laser beam passes through a 1024 × 768 transmissive spatial light modulator (Holoeye LC 2012, pixel size is 36 μm) with the phase profile of a blazed fork-shaped hologram that generates in the +1st diffraction order a vortex beam with the topological charge +2 or −2. Lenses L$_2$ ($f_2 = 150$ mm), L$_3$ ($f_3 = 150$ mm), and the diaphragm D constitute a 4-f system that makes the planes of the entrance pupil of the micro-objective MO$_1$ (100×, NA = 0.95) and of the light modulator conjugate. The polarizer P and the quarter-wave plate Q are used to convert the generated linearly polarized beam into a beam with left circular polarization. Using the second micro-objective MO$_2$ (100×, NA = 0.95), the intensity distribution of the focused vortex beam near the focus of the first micro-objective is imaged onto the matrix of the 3264 × 2448 CMOS camera ToupCam UCMOS08000KPB (pixel size is 1.67 μm). The optical resolution of a 0.95 numerical aperture lens is about 280 nm (0.5 λ/NA).

Figure 9 depicts transverse intensity distributions measured in the setup from Fig. 8 in the focal plane of a right-hand [Fig. 9(a)] and left-hand [Fig. 9(b)] circularly polarized optical vortex with the topological charge $m = 2$. Cross sections of these intensities are shown in Figs. 9(c) and 9(d). As seen in Fig. 9, the intensity on the optical axis ($x = 0$) is zero for right circular polarization [Fig. 9(c)], whereas for left circular polarization [Fig. 9(d)] it is nonzero. Distributions in Fig. 9 are overexposed to make the nonzero intensity near the optical axis clearly seen in Fig. 9(d).

The reverse flow cannot be measured in this experiment, since only that part of the intensity or power flow can be measured that goes into the MO$_2$ micro-objective in Fig. 8. It can only be stated that the intensity distributions in Figs. 6 and 9 are consistent. The difference between the simulation and the experiment (increased side lobes and reduced on-axis
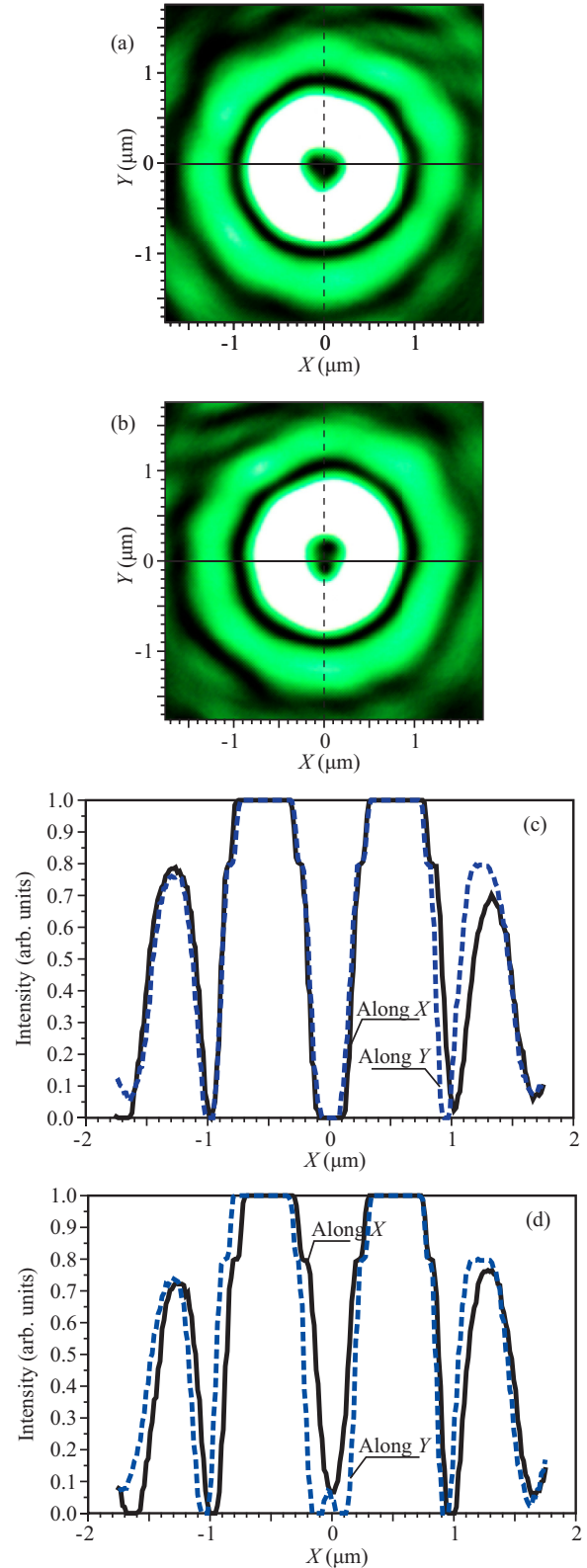

FIG. 9. Transverse intensity distributions measured in the focus of the right-hand (a) and left-hand (b) circularly polarized optical vortex with the topological charge $m = 2$, and corresponding intensity cross sections along the Cartesian axes (curve 1—along the axis x, curve 2—along the axis y) for right (c) and left (d) circular polarization. The size of 2D distributions (a,b) is $3.5 \times 3.5 \, \mu$m.
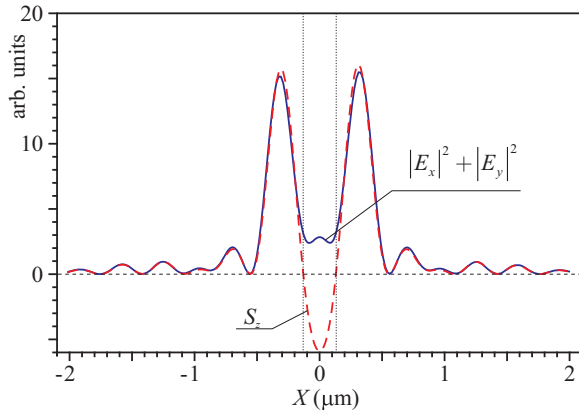
FIG. 10. Calculated distributions of intensity $|E_x|^2 + |E_y|^2$ and of the longitudinal component of the Poynting vector S_z in the focal plane of the left-hand circularly polarized optical vortex with the topological charge $n = 2$. All parameters are the same as in Figs. 6 and 7.

intensity) can be because the simulation was carried out for a diffractive lens (Figs. 6 and 7), whereas the experiment was made using refractive objectives (Fig. 8). Figure 9(d) demonstrates that the intensity near the optical axis is not axially symmetric. This is because the optical vortex with the topological charge of 2 is unstable and splits into two optical vortices with the topological charge of 1 [in Fig. 9(b); two isolated intensity nulls are on the vertical axis near the center of the pattern].

The intensity pattern near the optical axis in Fig. 9(d) is similar to that of the polarization vortex [Figs. 4(d) and 4(e)]. It is, though, interesting that because of the circular symmetry of the flow, the coordinates of the intensity nulls in Fig. 9(d) determine the diameter (distance between the zeros) of the reverse flow; that is, on the circle of this diameter (approximately 300 nm) the flow is zero. Similarly, in Fig. 4, the reverse flow for the second-order polarization vortex [Fig. 4(a)] has a diameter equal to the distance between the first two intensity nulls in Fig. 4(d) (approximately 300 nm). This follows directly from Eq. (23). It should not be surprising that the intensity is nonzero in the points with the zero reverse flow. The same effect is well known for the standing wave, whose flux is zero, but the intensity is nonzero.

Figure 10 shows calculated transverse distributions of the intensity $|E_x|^2 + |E_y|^2$ and of the longitudinal component of the Poynting vector S_z in the focal plane of the left-hand circularly polarized optical vortex with the topological charge $n = 2$. As seen in Fig. 10, the diameter of the circle with zero flux ($S_z = 0$) approximately coincides with the distance between the first two local intensity minima. In Fig. 10, this diameter is approximately 300 nm. The distance between the intensity nulls in the experimental picture [Fig. 9(d)] is also about 300 nm.

Near the focus and near the optical axis, energy flows propagate in the backward direction, whereas at some distance from the optical axis they propagate in the forward direction. In places where the forward and reverse flows converge (this occurs at the radii with the zero longitudinal component of the
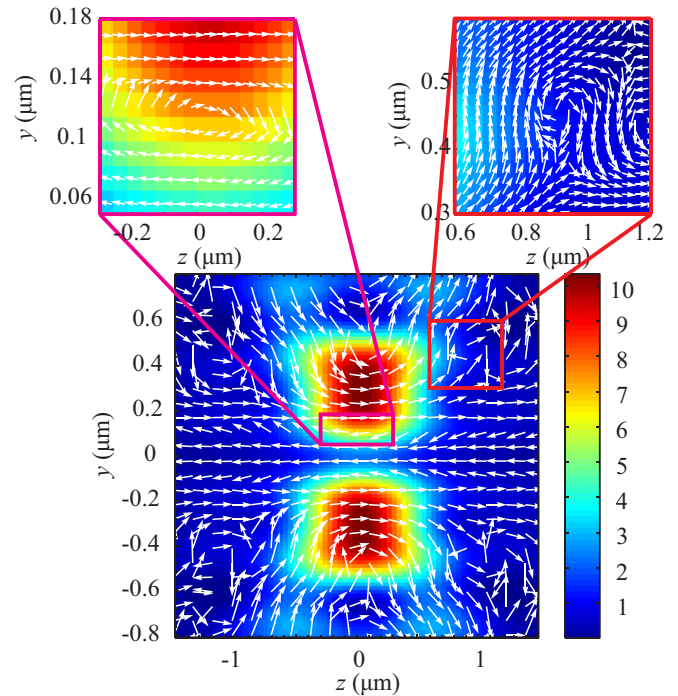

FIG. 11. Intensity distribution and directions of the Poynting vector (white arrows) in the longitudinal plane ZY when focusing an optical vortex with the topological charge $n = 3$ and with linear polarization.

Poynting vector, i.e., $\sqrt{2}I_{0,2}(r) = I_{2,0}(r)$), "optical whirls" or toroidal energy flows arise (Fig. 11).

According to Fig. 11, there is a toroidal vortex generated in the focal plane $z = 0$ (shown in the left upper inset in Fig. 10). The torus radius is approximately 0.3 μm. In planes distant from the focus (at distances $z = \pm 0.9 \, \mu$m $\cdots \pm 1.4 \, \mu$m), complex structured vortices are generated shown in the right upper inset in Fig. 11.

Figure 12 shows the result of another experiment performed in the setup from Fig. 8 with the spatial light modulator (SLM) replaced by a polarization plate, which converts linear polarization into second-order cylindrical polarization. Figures 12(a)–12(c) show the intensity distribution in the focus with a different degree of overexposure in order to visualize the low intensity near the center of the picture. Figure 12(d) shows cross sections of the overexposed intensity from Fig. 12(c) along the Cartesian axes. It is seen in Fig. 12(d) that in agreement with the theory predictions [Figs. 4(d) and 4(e)], there are two local minima (two isolated intensity nulls) near the optical axis in the focal plane of the beam with second-order cylindrical polarization. These intensity nulls [similar to those in Fig. 9(d)] make a boundary for the reverse energy flow and the distance between them equals the diameter of a tube with the reverse flow, about 300 nm in size.

In this experiment, an interesting feature is worth noting. It is important to clearly understand what specifically is registered in the experimental picture in Fig. 9. All the pictures in Figs. 6, 7, and 9 are of approximately the same size and
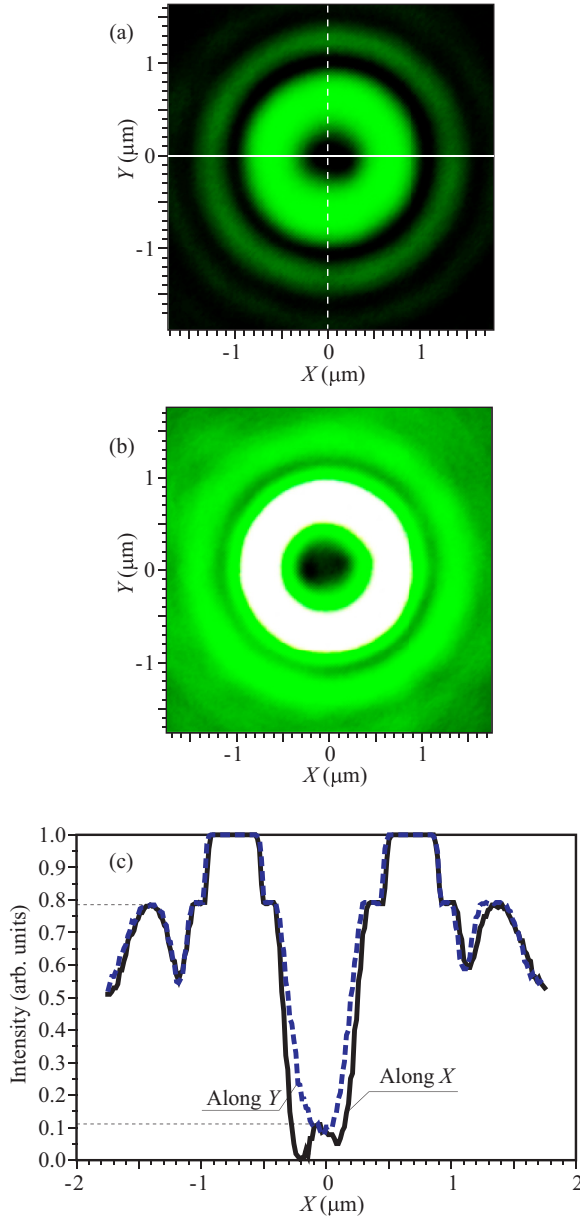
FIG. 12. Energy flow distribution (a,b), measured in the setup from Fig. 8 with the SLM replaced by the q-plate which converts linearly polarized light into polarization vortex. (a,b) have a different degree of overexposure in order to detect the nonzero flow in the center of the picture. The size of all pictures is $3.5 \times 3.5 \, \mu$m. (c) shows the intensity cross sections along the axes x and y.

circularly symmetric. In this case, it is impossible to determine exactly whether the transverse intensity distribution or energy flow was measured. This uncertainty is removed in the second experiment. The experimental picture in Fig. 12 is circularly symmetric in the focus, similar to the picture of energy flow [Fig. 4(c)], and differs from the transverse intensity distribution [Fig. 4(d)]. Therefore, the second experiment (Fig. 12) demonstrates unambiguously that the measured quantity is the energy flow distribution (its longitudinal component).

If there is reverse energy flow in the focus near the optical axis, then there should be zero values in the center of the measured energy distribution, since the reverse flow in the

focus does not go into the second micro-objective and thus cannot be measured. However, in the center of Fig. 12(c) there is a very small amount of energy (approximately $\frac{1}{8}$ of the side lobe). This part of the energy cannot be considered as intensity, since, as seen in Fig. 4(e), the intensity in the center should be about two times higher than the intensity of the side lobe. This energy cannot also be considered as intensified noise of the photoreceiver for there is no noise in the center of Fig. 9(c), although it is overexposed, so we need to know specifically what physical quantity is measured in the center of the energy flow distribution in Figs. 9(d) and 12(c).

The fact is that the second micro-objective MO_2 in Fig. 8 generates in its focus an image of the forward flow only. Therefore, in the center of this image there should be an area (about 300 nm in diameter) with zero flow. However, due to diffraction of the direct flow by this circle (similar to the diffraction by an opaque disk and and likewise the Arago spot), a local maximum appears in the center of the direct flow distribution, as in Fig. 12(c). Thus, the measured patterns of the axial component of the Poynting vector (Figs. 9 and 12) prove that there is reverse energy flow on the optical axis near the focus.

VI. FORCES EXERTED UPON A NANOPARTICLE IN REVERSE ENERGY FLOW

When placed in a light field, a nanoparticle experiences forces exerted upon it. For a Rayleigh nanoparticle, the force is composed of a dissipative and a gradient force. The Rayleigh particles with radius $a < \lambda/20$ experience the action of a dissipative force $\mathbf{F}_s$ and a gradient force $\mathbf{F}_g$, which are derived from the well-known formulas [37,38]:

$$\mathbf{F}_s = \mathbf{e}_z \left(\frac{8\pi n_2}{3c} \right) k^4 a^6 \left(\frac{n_1^2 - n_2^2}{n_1^2 + 2n_2^2} \right)^2 S_{or,z}, \qquad (37)$$

$$\mathbf{F}_g = \left(\frac{2\pi n_2}{c} \right) a^3 \left(\frac{n_1^2 - n_2^2}{n_1^2 + 2n_2^2} \right) \boldsymbol{\nabla} |\mathbf{E}|^2, \qquad (38)$$

where c is the speed of light in free space, a is the radius of a spherical Rayleigh particle, and n_1 and n_2 are the refractive indices of the particle and the medium. In Eq. (37), $S_{or,z}$ is the axial component of the orbital energy flow from Eq. (15). Equation (37) demonstrates that the scattering force, acting on a Rayleigh dielectric absorbing particle, placed on the optical axis in the energy backflow region, is directed in the same direction as light propagation. This means that the spin flow $\mathbf{S}_{sp}$ from Eq. (15), which is directed backward in the backflow region, does not affect the particle. In [34], an expression is given for the light force acting on a small conducting particle with the current, which is characterized by the conductivity σ:

$$\mathbf{F} = \frac{\sigma}{2} \text{Re}[\mathbf{E}^* \times \mathbf{H}]. \qquad (39)$$

Equation (39) was obtained in Ref. [34] under the condition that the electric Lorentz force equals zero and hence is suitable for a special type of particle. Equation (39) is valid for electrically neutral conductive particles. The electric current of electrically neutral MnS particles with a diameter of $4 \, \mu$m and a conductivity of $1.0 \times 10^7 \, (\Omega \, \text{m})^{-1}$ in a liquid was studied in [39].
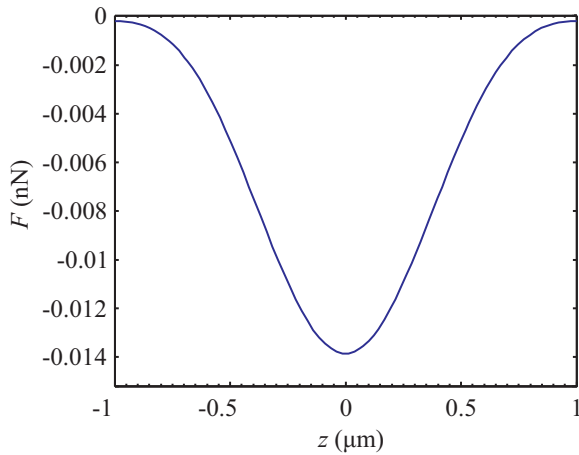
FIG. 13. Longitudinal components of force exerted along the optical axis ($r = 0$) on an electrically neutral conductive particle placed on the optical axis near the focus of a polarization vortex [Fig. 4(b)].

In this case, the particle is affected by both orbital $\mathbf{S}_{or}$ and spin $\mathbf{S}_{sp}$ energy flows (15). Figure 13 shows longitudinal components of force exerted along the optical axis ($r = 0$) on an electrically neutral conductive particle (radius $a = 10$ nm, wavelength $\lambda = 532$ nm) placed on the optical axis near the focus of a polarization vortex [Fig. 4(b)]. The original beam has a power of 100 mW, with the focusing performed for numerical aperture NA = 0.95. Conductivity, $\sigma = 1.0 \times 10^7 \, (\Omega \, \text{m})^{-1}$.

Using (21) and (22), we derive the longitudinal component S_z of the Poynting vector near the focus of a polarization vortex. Then, using (39), we derive the force exerted upon a nanoparticle (Fig. 13). The force (39) will push the nanoparticle in the negative direction along the z axis.

VII. CONCLUSIONS

Summing up, we have theoretically shown that analysis of the interference pattern of four plane waves with specially tailored linear polarization states indicates the presence of a reverse energy flow. Regions of the direct and reverse energy flows are staggered in the interference pattern. The magnitude of the reverse energy flow is in direct proportion to the angle of convergence of the plane waves (the angle of the wave vector with the optical axis), attaining its maximum at the convergence angle close to 90°. In some regions of the interference pattern, when summed up, the right-handed triplets $\mathbf{k}(k_z > 0)$, $\mathbf{E}$, and $\mathbf{H}$ generate an electromagnetic field described by a right-handed triplet $\mathbf{k}(k_z < 0)$, $\mathbf{E}$, and $\mathbf{H}$. These regions are characterized by the negative propagation of light. A similar explanation of the mechanism behind the generation of a reverse energy flow has been shown to apply to the case of focusing a second-order polarization vortex [Fig. 5(b)].

Using two identical micro-objectives with a numerical aperture of 0.95, it has been demonstrated experimentally that the intensity on the optical axis near the focus of an optical vortex with a topological charge of 2 is zero for right circular polarization and nonzero for left circular polarization. This confirms that in the latter case there is a reverse flow of light energy on the optical axis, since in the center of the measured energy flow distribution there is a very weak local maximum (the Arago spot) caused by diffraction of the forward flow by a circle 300 nm in diameter (the diameter of the tube with the reverse flow). Comparing the numerical and experimental intensity distributions, it is possible to determine the diameter of a "tube" with the reverse flow. It is equal to the distance between the first intensity nulls. For the numerical aperture 0.95 and the wavelength 532 nm, the diameter of the tube of the reverse flow along the optical axis is 300 nm.

In the areas where the reverse and forward flows "converge," optical whirls or toroidal energy flows appear.

It has also been calculated that a spherical conductivity nanoparticle placed in the reverse energy flow region experiences the action of a negative force.

[1] J. F. Nye and M. V. Berry, Proc. R. Soc. London, Ser. A **336**, 165 (1974).

[2] M. Soskin and M. Vasnetsov, in *Progress In Optics*, edited by E. Wolf (Elsevier, Amsterdam, 2001), pp. 219–276.

[3] G. A. Swartzlander, Jr., J. Opt. A: Pure Appl. Opt. **11**, 094022 (2009).

[4] K. T. Gahagan and G. A. Swartzlander, Opt. Lett. **21**, 827 (1996).

[5] M. Gecevičius, R. Drevinskas, M. Beresna, and P. G. Kazansky, Appl. Phys. Lett. **104**, 231110 (2014).

[6] N. B. Simpson, K. Dholakia, L. Allen, and M. J. Padgett, Opt. Lett. **22**, 52 (1997).

[7] K. Volke-Sepulveda, V. Garcés-Chávez, S. Chávez-Cerda, J. Arlt, and K. Dholakia, J. Opt. B **4**, S82 (2002).

[8] B. Thidé, H. Then, J. Sjöholm, K. Palmer, J. Bergman, T. D. Carozzi, Y. N. Istomin, N. H. Ibragimov, and R. Khamitova, Phys. Rev. Lett. **99**, 087701 (2007).

[9] A. Bandyopadhyay and R. P. Singh, Opt. Commun. **284**, 256 (2011).

[10] A. Bandyopadhyay, S. Prabhakar, and R. P. Singh, Phys. Lett. A **375**, 1926 (2011).

[11] B. J. McMorran, A. Agrawal, I. M. Anderson, A. A. Herzing, H. J. Lezec, J. J. McClelland, and J. Unguris, Science **331**, 192 (2011).

[12] V. V. Kotlyar, A. A. Kovalev, and A. G. Nalimov, Opt. Lett. **43**, 2921 (2018).

[13] V. V. Kotlyar, A. G. Nalimov, and A. A. Kovalev, J. Opt. **20**, 095603 (2018).

[14] V. V. Kotlyar, A. G. Nalimov, and S. S. Stafeev, Laser Phys. **28**, 126203 (2018).

[15] V. V. Kotlyar and A. G. Nalimov, J. Opt. **20**, 075101 (2018).

[16] B. Richards and E. Wolf, Proc. R. Soc. London, Ser. A **253**, 358 (1959).

[17] B. Z. Katsenelenbaum, J. Commun. Technol. Electron. **42**, 119 (1997).

[18] G. P. Karman, M. W. Beijersbergen, A. Van Duijl, and J. P. Woerdman, Opt. Lett. **22**, 1503 (1997).

[19] M. V. Berry, J. Mod. Opt. **45**, 1845 (1998).

[20] A. V. Volyar, Tech. Phys. Lett. **26**, 573 (2000).

[21] A. V. Volyar, V. G. Shvedov, and T. A. Fadeeva, Opt. Spectrosc. **91**, 235 (2001).

[22] M. V. Vasnetsov, V. N. Gorshkov, I. G. Marienko, and M. S. Soskin, Opt. Spectrosc. **88**, 260 (2000).

[23] A. V. Novitsky and D. V. Novitsky, J. Opt. Soc. Am. A **24**, 2844 (2007).

[24] S. Sukhov and A. Dogariu, Opt. Lett. **35**, 3847 (2010).

[25] C. W. Qiu, D. Palima, A. Novitsky, D. Gao, W. Ding, S. V. Zhukovsky, and J. Gluckstad, Nanophotonics **3**, 181 (2014).

[26] F. G. Mitri, J. Opt. Soc. Am. A **33**, 1661 (2016).

[27] M. A. Salem and H. Bağcı, Opt. Express **19**, 8526 (2011).

[28] P. Vaveliuk and O. Martinez-Matos, Opt. Express **20**, 26913 (2012).

[29] I. Rondón-Ojeda and F. Soto-Eguibar, Wave Motion **78**, 176 (2018).

[30] M. V. Berry, J. Phys. A: Math. Theor. **43**, 415302 (2010).

[31] W. T. M. Irvine and D. Bouwmeester, Nat. Phys. **4**, 716 (2008).

[32] D. Sugic and M. R. Dennis, J. Opt. Soc. Am. A **35**, 1987 (2018).

[33] H. Larocque, D. Sugic, D. Mortimer, A. J. Taylor, R. Fickler, R. W. Boyd, M. R. Dennis, and E. Karimi, Nat. Phys. **14**, 1079 (2018).

[34] M.V. Berry, J. Opt. A: Pure Appl. Opt. **11**, 094001 (2009).

[35] S. S. Stafeev, V. V. Kotlyar, A. G. Nalimov, and E. S. Kozlova, IEEE Photonics J. **11**, 4500810 (2019).

[36] V. V. Kotlyar, S. S. Stafeev, and A. G. Nalimov, Phys. Rev. A **99**, 033840 (2019).

[37] Y. Harada and T. Asakura, Opt. Commun. **124**, 529 (1996).

[38] A. Ya. Bekshaev, J. Opt. **15**, 044004 (2013).

[39] X. Zhang and R. Qin, Appl. Phys. Lett. **104**, 114106 (2014).